



# Measurement of temporal and spatial resolved rotational temperature in ignition sparks at atmospheric pressure

Tobias Michler<sup>1</sup> · Olaf Toedter<sup>1</sup> · Thomas Koch<sup>1</sup>

Received: 19 September 2019 / Accepted: 21 March 2020 / Published online: 29 March 2020  
© The Author(s) 2020

## Abstract

In this work, the temporal and spatial rotational temperature, as an indicator of spark temperature in the gas, of an ignition spark at ambient pressure is determined. With optical emission spectroscopy, the rotational bands of the nitrogen  $C^3\Pi_u \rightarrow B^3\Pi_g$  transition at a wavelength of 337 nm are for determination. In addition, the electrical values of the current and the voltage are measured with a digital storage oscilloscope. All measurements are performed with a common nickel spark plug and a commercial 90 mJ ignition coil. The dwell time of the coil is varied in four steps from 100 to 25% and the influence on the rotational temperature is measured. The results are split into the three spark phases: breakdown, arc discharge, and glow discharge. The results show a cold breakdown, which is independent from the dwell time. On average, arc discharge is the hottest discharge phase, while the glow discharge has a medium rotational temperature.

**Keywords** Spark Temperature · Spark phases · Ignition · Arc phase · Glow phase · Breakdown

## Abbreviations

CCD	Charge-coupled device
FDS	Faraday dark space
LTE	Local thermal equilibrium
NG	Negative glow
OES	Optical emission spectroscopy
PC	Positive column
PTG	Programmable timing generator
SI	Spark ignition
SNR	Signal-to-noise ratio
SPS	Second positive system

## 1 Introduction

The contribution of CO<sub>2</sub> emissions of anthropogenic sources, especially of individual mobility, to the global warming is being discussed more than ever in public and politics. Therefore, the European Union defined a climate

target, which is a 40% CO<sub>2</sub> reduction of greenhouse gases from anthropogenic sources by the year 2030 (compared to the year 1990) [16]. In addition, a long-term climate target of a 80% greenhouse gas reduction by 2050 was publicized in 2018 [17]. Also [31] showed that in 2030, vehicles with internal combustion engines will be the majority.

Therefore, a continuous improvement of SI engines in terms of efficiency is important for the future, both, with fossil and regenerative fuels. Possible solutions could be lean or diluted mixtures [1, 53] as well as pre-chamber spark plugs [63, 64], which increase the efficiency of internal combustion engines. The three options mentioned are increasing the stress on the spark plug in terms of inflammation probability and wear [9, 11, 69].

Therefore, the knowledge of the inflammation processes and spark plug wear have to be improved further. For this reason, we applied a technique for determination of spatial and temporal resolved plasma analysis by optical emission spectroscopy (OES) of the ignition spark. In this paper, results of the calculation of rotational temperature as an indicator of spark temperature at atmospheric pressure and room temperature by variation of the ignition coil dwell time are shown.

✉ Tobias Michler  
tobias.michler@kit.edu

Olaf Toedter  
olaf.toedter@kit.edu

<sup>1</sup> Institut für Kolbenmaschinen (IFKM), Karlsruher Institut für Technologie (KIT), Kaiserstraße 12, 76131 Karlsruhe, Germany

### 1.1 Theory of the ignition sparks

Rudolf Maly investigated the plasma of the ignition systems in the 1970s and 80s in several publications. He observed three different kinds of discharges in the ignition spark: the breakdown, the arc discharge and the glow discharge [39, 41]. These three phases behave differently in respect to the inflammation probability which Fig. 1 shows [40]. In this graphic with the same amount of energy, the breakdown phase is the best for the inflammation of lean air–fuel mixtures. It is followed by the arc. The worst inflammation probability has the glow discharge.

#### 1.1.1 Theory of the breakdown

The breakdown is the initial start to create the conductive channel of the ignition spark plasma. To form this channel, a voltage, which can be described by Eq. (1), is needed [49]

$$U_Z = \frac{B \times p \times d}{\ln\left(\frac{A \times p \times d}{\ln\left(1 + \frac{1}{\gamma}\right)}\right)} \tag{1}$$

where the breakdown voltage is  $U_Z$ , the constants are  $A$  and  $B$  which are fitting parameters, the pressure is  $p$ , the distance between the electrodes is  $d$  and the third townsend coefficient is  $\gamma$ . According to this equation, the breakdown voltage depends only on the product of pressure and distance as well as the medium.

The channel development starts by a first single electron. This electron will collide with atoms or molecules in the air. Because of the exponential characteristic of this discharge, it is called Townsend or avalanche discharge. Once the electron has accumulated enough energy, it is able to release another electron from the collision partner. The electron number follows the trend of Eq. (2) [65–67]:

$$\gamma \times (\exp^{\alpha \times d} - 1) \geq 1 \tag{2}$$

where the third Townsend coefficient is  $\gamma$ , the first Townsend coefficient is  $\alpha$ , and the electrode gap is  $d$ . If a critical

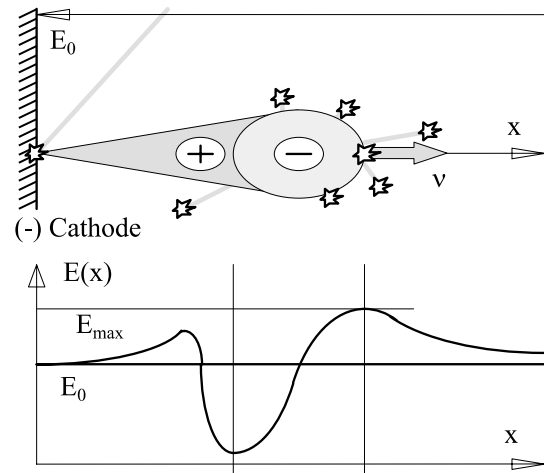


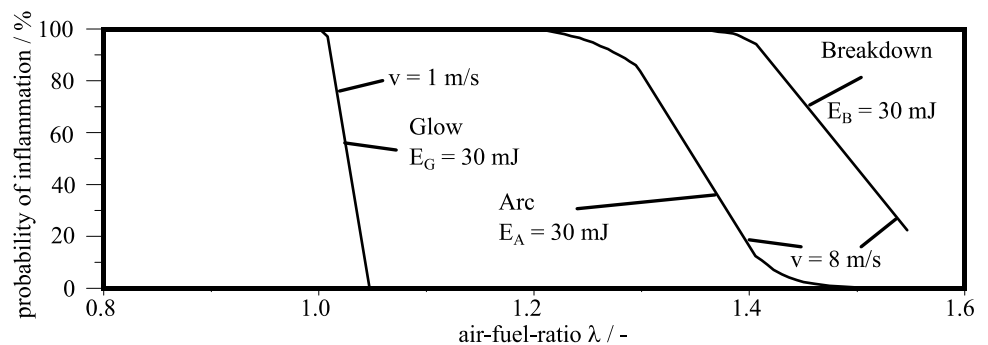
Fig. 2 Schematic of streamer formation [32]

electron number is achieved, the townsend discharge changes to a streamer discharge, which is described by [37, 43, 54]. In this discharge, three differently charged areas (positively charged, negatively charged, neutral) occur within the spark gap, like Fig. 2 shows. The fast electrons form the negative streamer head. The slow ions form the streamer tail. The electric field near the streamer head is amplified. This leads to an increase of the collision processes and therefore an increase in radiation. The duration of the breakdown is short and in the range of  $10^{-8}$  s [57].

#### 1.1.2 Theory of the arc phase

Arcs are the so-called thermionic, field, or the combination thermionic–field discharges [18]. In case of spark plugs, a thermionic or thermionic–field discharge is the most common. This depends on the cathode material when looking at the boiling points of the materials [21]. In this case the electrons of the discharge are released by the high temperature of a small spot, the so-called cathode [6, 24, 58]. The current density can be described by the Richardson–Dushman Eq (3) [13, 33]:

Fig. 1 Influence of the different discharge types of the ignition spark on the probability of inflammation at different air–fuel ratios [40]



$$j = A_r \times T^2 \times \exp\left(-\frac{e\phi}{k_B T}\right) \tag{3}$$

In this equation,  $j$  is the current density,  $A_r$  is the area of the cathode spot,  $T$  is the temperature,  $e$  is the elementary charge,  $\phi$  is the working function of the cathode material, and the Boltzmann constant is  $k_B$ . For many materials, the boiling temperature of the cathode material is too low for the needed electron current density [47]. On the other side, metallic damp in a short distance of the cathode that can produce high electric field strength [38, 56]. In this case, the Schottky effect can increase the number of electrons released by temperature using the tunnel effect by reducing the working function of the cathode material [59].

Due to the thermionic and thermionic–field emission, no strong electric field is needed. The needed voltage over the cathode fall area is in the range of about 10–20 V [5]. Since the electrons are provided by the heated cathode, the energy of these electrons is also high near the cathode. In case of spark plugs, the positive column takes up almost the entire distance between the electrodes. Within this column, the constant electric field accelerates the electrons, which can collide with other particles and transfer their energy [18].

### 1.1.3 Theory of the glow discharge

The main difference to the arc discharge is the way of providing electrons. By collisions of electrons, ions or excited atoms, more of these particles can be produced by the effects described above. Slow ions accumulate at the front of the

cathode and form together with medium-fast electrons, which are present in a high amount, the negative glow (NG) [18]. In this area, high radiation by recombination of electrons with ions can be observed. In addition, the ions produce a strong electric field between the ions and the cathode. This field results in the so-called cathode fall of the glow discharge and is in the range of several hundred volts [23, 25]. The process of recombination and collisions decreases the number of electrons and their energy. Therefore, further excitation by electron collisions after the NG can only be observed to a small degree. The further the electrons travel through the electric field, the more energy they can accumulate until they have enough energy to excite and ionize the gas. These parts of the glow discharge are referred to as the Faraday dark space (FDS) and, as with the arc discharge, also as the positive column (PC).

## 1.2 Electrical structure of the spark plug and the ignition system

The supplied energy of the ignition spark depends strongly on the electrical properties of the total ignition system. Therefore, a good understanding of the basic structure of the system, which is shown in Fig. 3, is of major importance. In general, the system consists of two inductors ( $L_{prim}$  and  $L_{sec}$ ), three resistors ( $R_{prim}$ ,  $R_{Coil}$  and  $R_{SP}$ ), and several, mostly parasitic, capacitors ( $C_{Coil}$ ,  $C_{Cable}$ ,  $C_{SP1}$  and  $C_{SP2}$ ). The two capacitors in the spark plug, which are separated by the interference suppression resistor, are resulting from

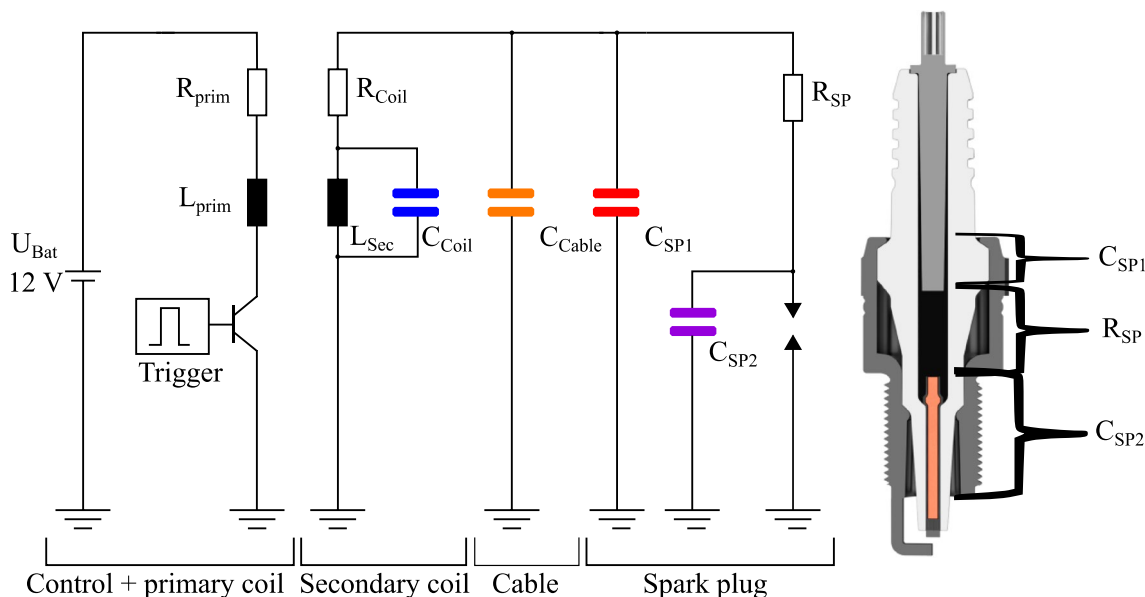


**Fig. 3** Schematic illustration of the ignition system in accordance with [55]. On the left side, the total ignition system with primary and secondary part of the coil, the ignition cable, and the spark plug.

On the right side, a CAD image of a spark plug with the delineated parasitic capacitors and the suppressor resistor

the potential difference between the center electrode and the grounded metal housing separated by the ceramic insulator.

Each discharge phase of the plasma is controlled by the electrical components of the ignition system. Only the lower capacitor of the spark plug ( $C_{SP2}$ ) can discharge during the breakdown phase due to its short RC time constant. The combination of a low capacity  $C$  of approx.  $10^{-11}$  pF and the relatively low resistance  $R$  of the plasma channel in the breakdown (approx.  $10^2 \Omega$ ) lead to the time constant  $\tau$  of this system, which is in the order of  $10^1$  ns [57]. This relation is shown by the following Eq. (4):

$$\tau = R \times C. \tag{4}$$

The capacitors, whose discharge is inhibited by the suppression resistor, supply an arc discharge, which was proven in earlier investigations [45]. Because of its energy source, this phase is called capacitive arc discharge. If the current of the discharge in the inductive discharge phase is high enough, an instable arc can be observed

[8]. To differentiate this instable arc from the very stable capacitive arc, it is called inductive arc discharge. When the current decreases further, a glow discharge solidifies. Table 1 gives an overview of the relationships described.

## 2 Experimental setup and methodology

All tests are performed under atmospheric pressure (1 bar) and at a temperature of approximately 300 K. To protect the investigation of interfering light influences, caused by scattered sunlight from the walls, and the ceiling lightning, the entire optical test setup is placed in a blackened metal box and covered with a black cloth.

### 2.1 Optical emission spectroscopy

The used test setup is shown in Fig. 4. This setup was used by us in previous works [30, 46].

**Table 1** Overview of the energy source of the discharge, the physical discharge mechanism, and our nomenclature [45]

Capacitors		Inductors	
Breakdown	Arc discharge		Glow discharge
	Capacitive arc discharge	Inductive arc discharge	

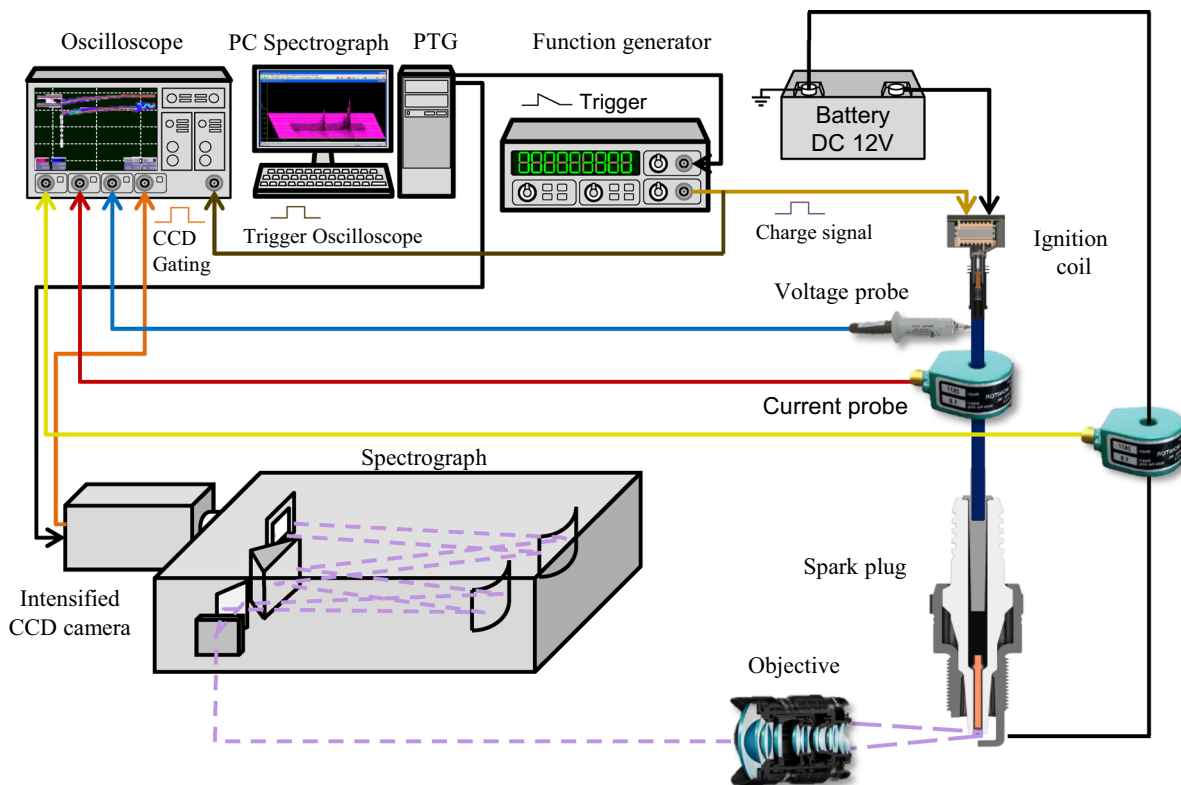


**Fig. 4** Schematic illustration of the optical and electrical test setup of the signal and trigger chain

A 12 V car battery is used as the voltage source of the ignition system. The ignition coil is a field-proved standard 90 mJ cassette coil. In this setup, only one of the coils is used. A standard spark plug with an electrode gap of 0.9 mm and a center electrode diameter of 2.5 mm are used. The cathode material is a common nickel alloy. The spark plug has a suppressor resistor of 6.5 k $\Omega$ , an overall capacity of 12.5 pF, and an inductivity of 530  $\mu$ H. Compared to the high inductance of the secondary side, which is in the order of  $10^1$  H [7], the inductance of the spark plug is negligible.

A LeCroy Waverunner 6030A digital storage oscilloscope with four input channels is used to record the electrical signals. It has a cutoff frequency of 350 MHz, a maximum sample rate of 2.5 GS/s (when more than two channels are used), and a rise time of 1 ns. The measurement frequency is set to 10 MS/s and is limited by the memory speed and the size of the data files. To measure the voltage on the high voltage side, a Tektronix P6015A high voltage probe with a cutoff frequency of 75 MHz and a rise time of 4.67 ns is equipped. This high voltage probe is connected via the corresponding compensation box to the oscilloscope (blue line). After the voltage probe, a Pearson 2877 current monitor is located (red line). This current clamp has a lower and upper cut of frequency of 300 Hz and 200 MHz, respectively. The rise time is about 2 ns. A second current clamp (yellow line) of the same type is placed in the ground path (black line from spark plug to the ground of the battery) of the ignition system. The charge signal of the coil (bright brown line) is provided by a function generator Hameg HM8130. This signal is additionally used as the trigger signal for the oscilloscope (dark brown line).

For the optical emission spectroscopy (OES), an Acton SP2556 from Princeton Instruments (focal length of 500 mm) is used. The spectrograph has three different gratings (150 grooves/mm, 600 grooves/mm and 1200 grooves/mm) mounted on a turret. In these investigations, only the 600 grooves/mm grating is used. The entrance slit of the spectrograph is set to 200  $\mu$ m. The intensified CCD camera, mounted on the spectrograph, is a Princeton Instruments PI-MAX 2 with a full-size resolution of  $1024 \times 256$  pixels. In combination with the 600 grooves/mm grating, the detector coverage is approx. 85 nm. Therefrom, the resolution of this combination is in the order of 0.08 nm. Both, the camera and the spectrograph, are operated via the spectrograph's PC (PC spectrograph) with the software Winspec. To collect the light from the plasma (violet lines) of the ignition spark, a Hamamatsu A4869 UV-objective is used. With a low-pressure mercury argon lamp (LOT-Oriel LSP035) as reference, the half-width was calculated to be 4.9  $\text{\AA}$ .

From the software, the initial trigger is sent to the programmable timing generator (PTG). The PTG transmits a signal to the function generator, to trigger the charge signal of the ignition coil, and the camera (black lines). The signal

of the open gate from camera (orange line) is sent to the oscilloscope. Therefore, the timing of the camera can be fitted to the electrical signals of the ignition spark.

The measurement is fully automated. In these experiments, two different gate opening durations are used. A gate opening duration of 0.5  $\mu$ s is used for the breakdown, 10  $\mu$ s are used for the first 100  $\mu$ s. From 100  $\mu$ s to the end of the spark, the gate opening duration is at 100  $\mu$ s. At every gate opening time, 20 measurements and three differently focused wavelengths (340 nm, 380 nm, and 780 nm) are recorded. After these 60 measurements, the gate timing is delayed by the length of the gate opening duration. This procedure continues until the end of the ignition spark. The validation of these timing and gate durations not to influence measurement results was presented in [30, 46].

## 2.2 Electrical evaluation

The evaluation of the electrical signal is carried out by a MATLAB script. Using an algorithm that uses the voltage and the current signals to detect even short transitions, the electric energy and the duration of the arc and the glow discharge can be calculated.

The energy of the arc and the glow discharge is calculated by Eq. (5):

$$E_{el} = \int_{tbd}^{ted} (u(t) \times i(t)) dt \quad (5)$$

where the electrical energy is  $E_{el}$ , the start and the end time of the discharge are  $tbd$  and  $ted$ , respectively, the voltage is  $u(t)$  corrected due to the losses by the spark plug resistance, and the secondary current is  $i(t)$  of the first current probe. The correction of the voltage is carried out by Eq. (6):

$$u(t) = R_{SP} \times i(t)^2 \quad (6)$$

Where  $R_{SP}$  is the suppression resistor of the spark plug. Because of the very short duration of the breakdown, its energy  $E_B$  can be calculated by Eq. (7):

$$E_B = \frac{1}{2} \times U_Z^2 \times C_{SP2} \quad (7)$$

where  $U_Z$  is the maximum peak voltage before the breakdown and  $C_{SP2}$  is the lower capacitor of the spark plug, which is in this case 8.33 pF (approx. 2/3 of the total spark plug capacity of 12.5 pF).

A persistent plot of 400 sparks is shown in Fig. 5. The two phases of the inductive arc and the glow discharge are clearly separated by the two voltage levels in the first 200  $\mu$ s of the discharge. The difference between these

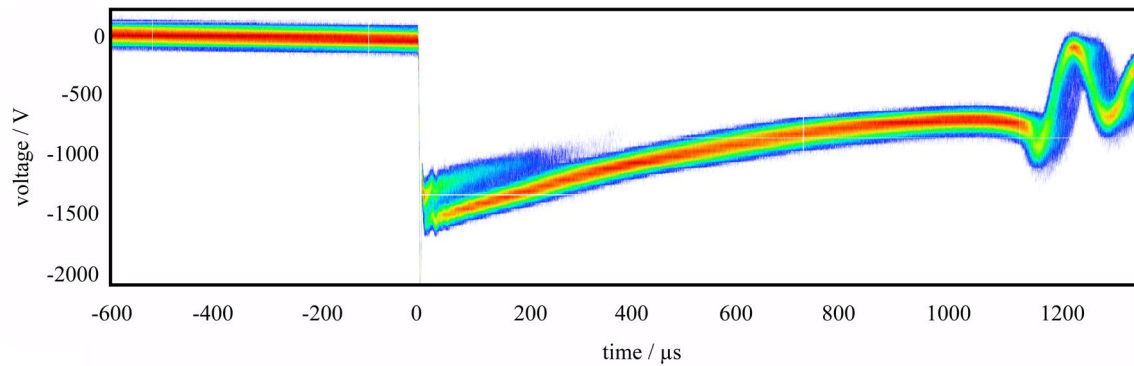


**Fig. 5** Persistent plot of 400 measurements of the secondary high voltage. The red color denotes high density of datapoints. Shortly after the breakdown, the two different voltage levels of arc and glow discharge are observed

levels is approx. 300 V, which is the difference in cathode fall between the two discharge types. The breakdown has a cutoff and is in the range of 5000 V

### 2.3 Measurement of the rotational temperature

The rotational temperature is often used to estimate the temperature of the gas [48, 61]. In Fig. 6a, a schematic example of the formation of the rotational bands of nitrogen is given. The black lines mark the electronic states. In blue, the vibrational levels within the electronic levels are marked and are numerated. The different rotational levels of a vibrational state are shown in red.

The energy difference between the electronically excited states is by far the largest in this example. Within the vibrational excited states, a much smaller energy difference is observed. The smallest difference of the energy is within the rotational levels. This relation between the energy levels leads to the following spectrum shown in Fig. 6b. In this figure only, the transition of the electronic excited state  $C^3\Pi_u \rightarrow B^3\Pi_g$ , the second positive system of nitrogen (SPS), is present. The transitions of the vibrational states are shown as the small numerated peaks. The  $v'$  is the number of the upper vibrational level and  $\Delta v$  is the difference between the number of the upper and lower vibrational level. The rotational level can be observed by the shape of the intensity

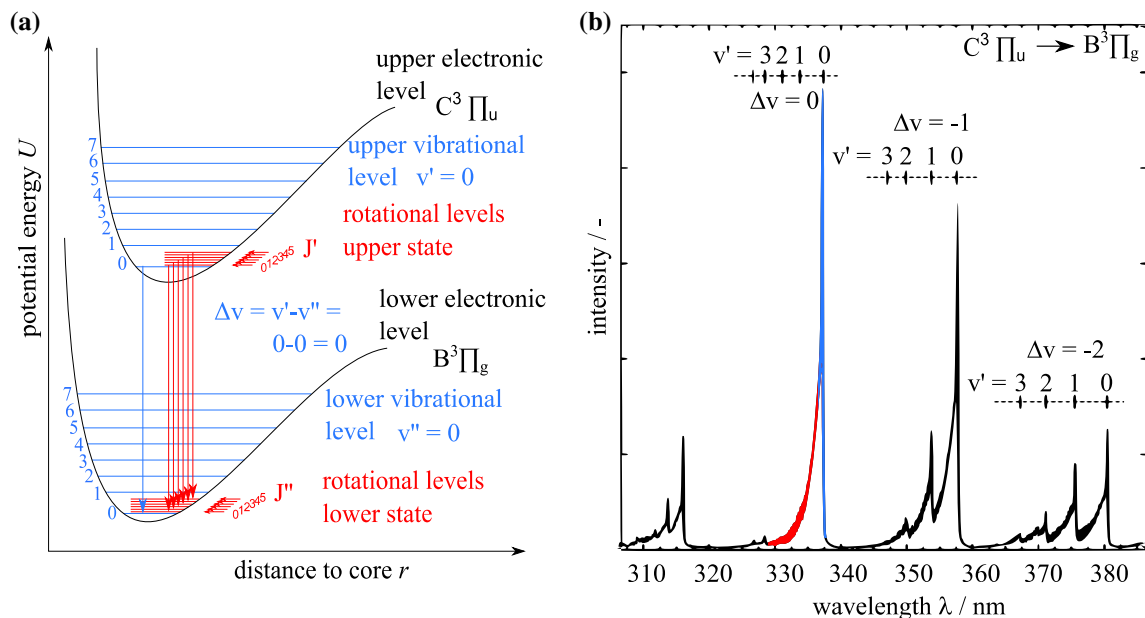


**Fig. 6** Schematic energy levels of nitrogen SPS system **a** with respect to the electronic levels (black), the vibrational levels (blue), and the rotational levels (red). **b** Measurement example of the SPS in the

wavelength range of 310–380 nm. For estimation of the rotational temperature, the nitrogen SPS  $\Delta v=0$  band system, with a band head of 337 nm is used

between two vibrational levels at a constant  $\Delta v$ . Because of the too low resolution of the optical system, these rotational bands cannot be disbandled by the spectrograph, but the shapes of the bands are clearly visible.

For calculating the rotational temperature, the following transition, which is shown in Eq. (8), in a wavelength range between 320 and 337.1 nm is used:

$$C^3 \prod_{u'} v' = 0 \rightarrow B^3 \prod_{g'} v' = 0 \quad (8)$$

The temperature calculation by the unresolved band shape is a common procedure [10, 27, 36, 50, 52]. The difference between resolved and unresolved rotational bands of the  $C^3\Pi_u \rightarrow B^3\Pi_g$   $\Delta v=0$  is shown in Fig. 7. In the upper graph, the peaks of the rotational levels are clearly visible. The lower graph shows a smoother continuous line. To calculate the temperature, a pool of approx. 11,000 simulations between a rotational temperature of 300 K to 6000 K  $\pm$  and a vibrational temperature between 500 and 10,000 K is generated. The simulations are created by the open source MATLAB code Spartan 2.6 [34, 35]. Because of the small observation volume of each camera pixel row (which is the height dimension of the ignition spark), a local thermal equilibrium (LTE) is assumed. The spectroscopic measurements of each time step and pixel row are averaged over 20 measurements. Thereafter, the measured spectra are compared with each simulated spectrum by a cross-correlation.

The error is the sum of the resolution of the simulation steps (in this case  $\pm 50$  K) and the influence of the

signal-to-noise ratio (SNR). To calculate the uncertainty due to noise, three simulated spectra with different rotational temperatures are used (450 K, 2300 K and 4600 K). These spectra are superimposed by eight noise strengths (5%, 10%, 15%, 20%, 25%, 30%, 40% and 50%). The noise is calculated by Gaussian distributed random numbers between zero and one, which are multiplied by the signal and a random sign. Thereafter, the noise is summed up with the simulated spectra. These noisy spectra are entered into the temperature calculation tool. The results of the uncertainty of a SNR of 50% and the overall uncertainty are shown in Table 2.

## 3 Results

### 3.1 Overview

The overview of the electrically supplied energy and the duration of the three different discharge modes is given in Table 3. The breakdown is not affected by different dwell

**Table 2** Exemplary measurement uncertainty due to the SNR of 50% at different rotational temperatures

Rotational temperature/K	Uncertainty due to SNR/K	Uncertainty/K
450	50	100
2300	200	250
4600	250	300

**Fig. 7** Simulated spectra of the  $C^3\Pi_u \rightarrow B^3\Pi_g$   $\Delta v=0$  rotational band system. In the upper graph the resolved rotational bands with a half-width of 0.1 Å. The lower graph shows the unresolved rotational band with a half-width of 4.9 Å

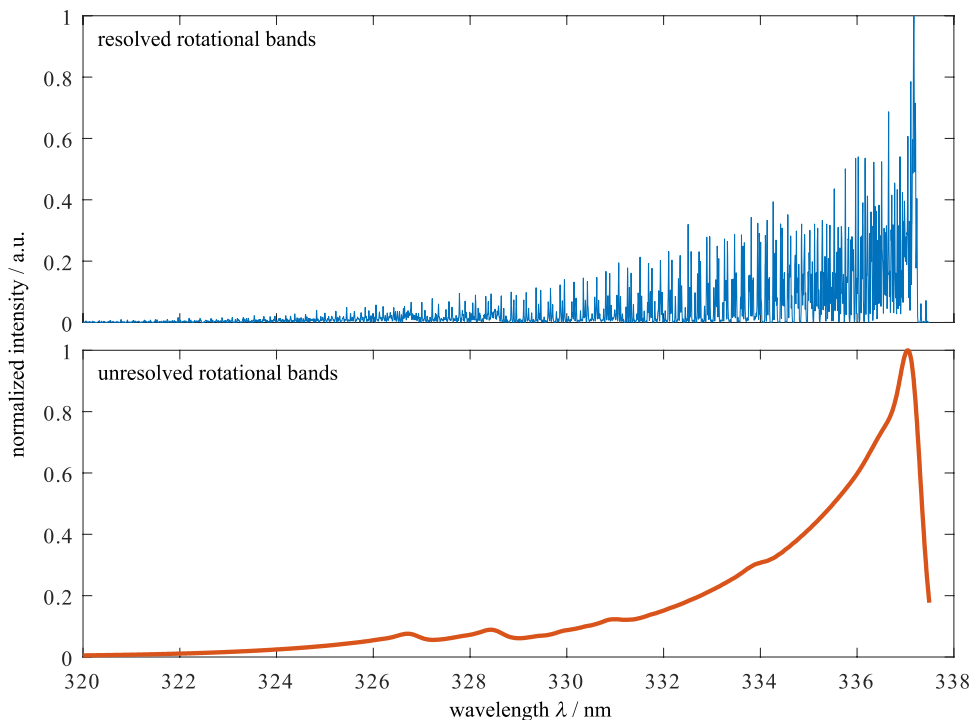


**Table 3** Overview of the electrically supplied energy and the duration of the three different discharge modes

Dwell time/ %	Breakdown energy/mJ	Arc energy/mJ	Arc duration/ $\mu$ s	Glow energy/mJ	Glow duration/ $\mu$ s
25	0.1	0.1	2	4.7	528.4
50	0.1	0.2	7.7	12.1	927.3
75	0.1	0.8	15.0	16.8	1056.5
100	0.1	3.9	47.3	18.8	1018.7

times and has an energy of approx. 0.1 mJ in this configuration. The breakdown voltage is in the range of 4.5–5.5 kV for all four dwell times. In arc mode, which is the sum of inductive and capacitive arc mode in the table, the dwell time has a significant influence, especially from 100% down to 75% dwell time, and decreases from 3.9 to 0.8 mJ. This is also caused by a shorter duration of the arc mode at smaller dwell times. At 50% dwell time, the inductive arc mode occurs only sporadically and the duration and the energy decreases again. At the smallest dwell time, the arc mode is mostly the capacitive arc mode, which cannot be prevented. The decrease in inductive arc mode correlates with the decrease of the starting current of the inductive discharge by decreasing the dwell time. The glow energy behaves similar to the arc energy and decreases from 18.8 to 4.7 mJ. Only the duration of the glow discharge behaves different at 100% and 75% dwell time. In this case, a slight increase in glow discharge by decreasing the dwell time is observed. This might be an effect of the lower starting current and therefore the lower probability for an inductive arc discharge. In this case, the discharge will spend more time in the glow discharge than in the arc discharge.

Figure 8 shows the overview of the measured rotational temperature over the distance from cathode and the spark duration by varying the dwell time. The different dwell times show a similar trend. At the cathode a hot area with a temperature of approx. 4000 K is measured. This is followed by the NG with its typical high intensity values. This area has a colder rotational temperature compared to the cathode near area. Afterwards, a rise in the rotational temperature to 3000 K is observed in the PC area. In between these two areas the Faraday dark space (FDS) is located [22, 26]. With decreasing current, the temperature in the NG and the PC of the glow discharge decreases slightly. The breakdown and the arc discharges are not clearly visible in this figure. For reasons of clarity, the phases are averaged over the time and plotted against the distance between cathode and the anode in further discussion.

In addition to the rotational temperature, the intensity of radiation, and thus the density of excited molecules, has to be observed. For better comparison, the intensity of the  $C^3\Pi_u \rightarrow B^3\Pi_g$ ,  $\Delta v=0$  band head at 337 nm in Fig. 9 is summed up over the discharge gap for every time step. In the breakdown, the summed intensity is for all dwell times

the highest. It is independent from the dwell time. The differences in the intensity result from statistical phenomena of breakdown voltage and therefore a slight difference of the breakdown energy. Also, the short gate opening duration of 500 ns and the different spatial position of the breakdown on the cathode influence this intensity. Immediately after the breakdown, the emission intensity drops strongly to approx. 20% of breakdown intensity. The four dwell times are clearly separated. The summed intensity decreases with the dwell time and with each time step, and therefore with the current, of the discharge.

### 3.2 Rotational temperature of the breakdown

The rotational temperature of the breakdown is shown in Fig. 10. The temperature near the cathode is with a range of 1650–2150 K the highest. In this temperature range, the error is about 250 K like it is shown before. Afterwards, the rotational temperature decreases to  $450 \text{ K} \pm 100 \text{ K}$  in average over the discharge gap. This temperature range is in good agreement with the rotational temperature found by [60]. These rotational temperatures are independent from the dwell time. The breakdown is measured with a gate duration of 0.5  $\mu$ s. This is 50 times the duration of a 10 ns breakdown. Therefore, not only the breakdown is in this temperature calculation, but the calculation is strongly dominated by it due to its high intensity of radiation. We have observed that with longer gate durations during the measurement of the breakdown, the average determined rotational temperature also increases. So, it is most probable that the breakdown has a lower temperature in the range of the room temperature of 300 K.

### 3.3 Rotational temperature of the arc phase

As discussed in the section before, the only measurement with a pronounced arc phase is the measurement at a dwell time of 100%. All dwell times have similar rotational temperatures in the range of 3550 K to 3950 K  $\pm 300 \text{ K}$  with regard to the measurement uncertainty near the cathode, as it is shown in Fig. 11. The temperature distribution in this area does not depend on the dwell time. After this area, from 0.1 to 0.4 mm, the temperature of the 100% dwell time is the hottest with approx. 2700 K  $\pm 250 \text{ K}$ . The coldest plasma in

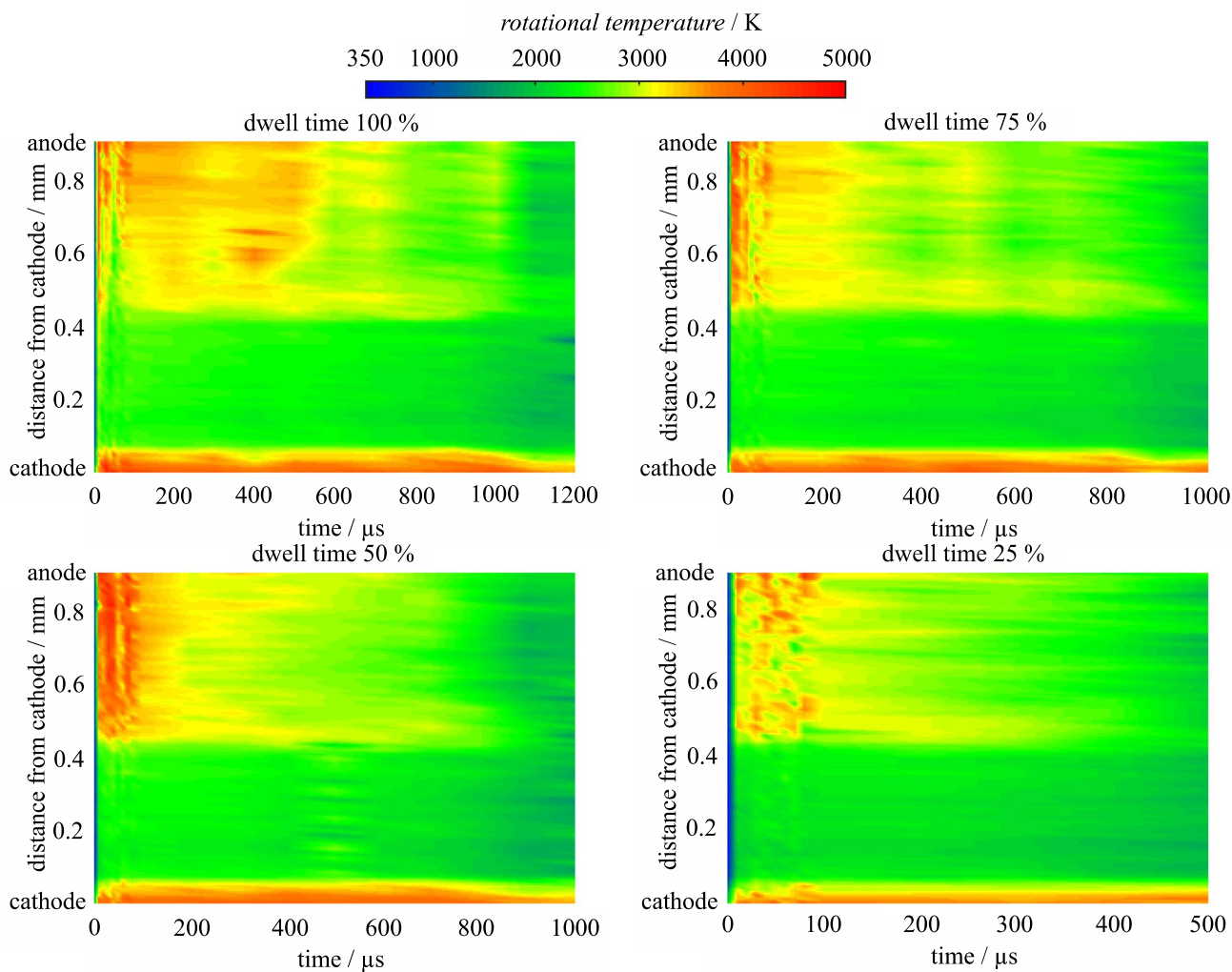
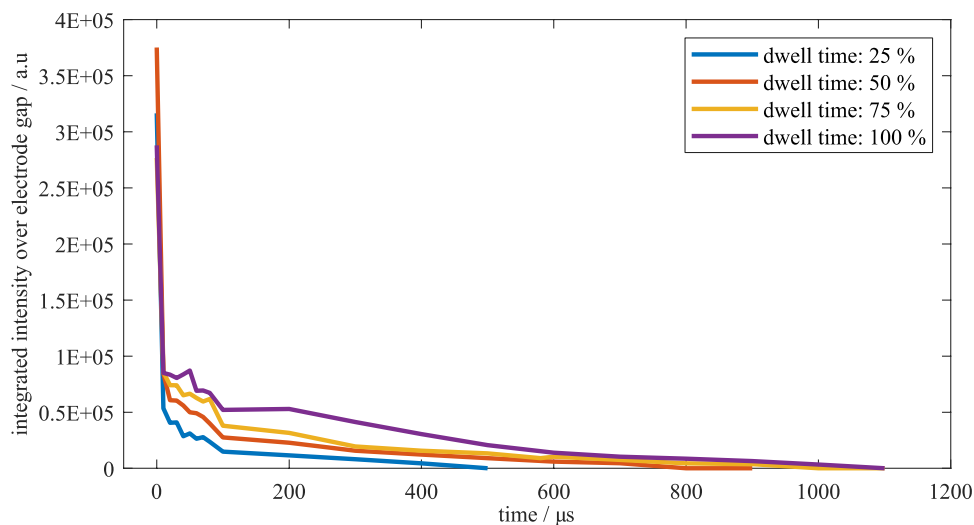


**Fig. 8** Overview of the calculated rotational temperature by variation of the ignition coil dwell time

**Fig. 9** Above the electrode gap integrated intensity of radiation, of the  $C^3\Pi_u \rightarrow B^3\Pi_g \Delta v=0$  band head at 337 nm, for the four dwell times



this distance area, with a temperature of  $2140 \text{ K} \pm 250 \text{ K}$ , is at the shortest dwell time of 25%.

The plasma of the 25%, 50%, and 75% is dominated by effects of the glow discharge due to the short arc phase duration in these experiments (showed in Table 3). This is clearly shown by the intensity of radiation trends of the measurements. Even in this early phase of the spark, the energy of the arc discharges is small compared to the energy of the glow discharge. Therefore, only in the 100% dwell time measurement residues of the arc are evaluated. Following the cold area, the temperature increases in a distance from 0.4 mm to 0.5 mm after the cathode. The 100% dwell time measurement has the smallest slope and the temperature increases from 2900 to 3400 K, in comparison to the other slopes from

approx. 2500–3600 K. In the upper part of the spark, from 0.5 mm to the anode, the temperature is on a plateau. In this case the 100% dwell time is in the range of  $3500 \text{ K} \pm 300 \text{ K}$ . The 75% and 50% dwell time show the highest temperatures of  $3900 \text{ K} \pm 300 \text{ K}$  and  $4000 \text{ K} \pm 300 \text{ K}$ . With a temperature of  $3300 \text{ K} \pm 250 \text{ K}$ , the 25% dwell time is the coldest.

### 3.4 Rotational temperature of the glow discharge

Directly at the cathode, the rotational temperature of the glow discharge has its maximum between 3750 K and 4100 K  $\pm 300 \text{ K}$ , as it is shown in Fig. 12. With increasing the distance from the cathode, the rotational temperature decreases to constant values of approx. 2200 K and

**Fig. 10** Rotational temperature during the breakdown phase at different positions in the discharge gap by varying the dwell time of the ignition coil

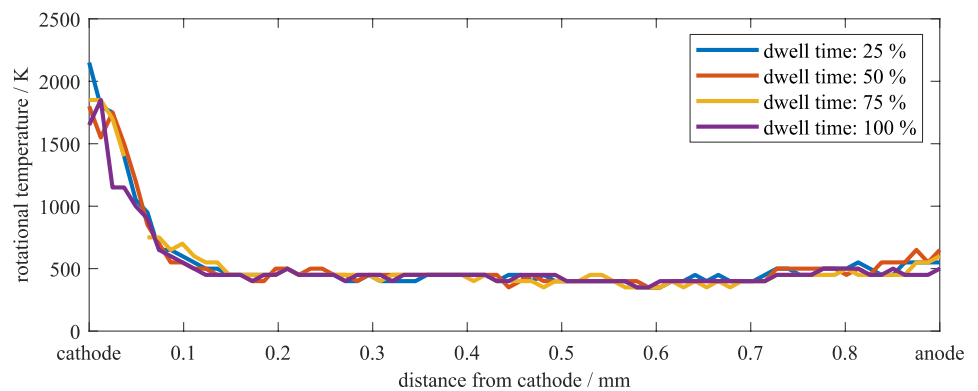


**Fig. 11** Rotational temperature during the arc phase at different positions in the discharge gap by varying the dwell time of the ignition coil. Only the 100% dwell time shows a relatively long inductive arc phase of approx. 30  $\mu\text{s}$ . The other dwell times are dominated by the glow discharge. Only the capacitive arc phase occurs in these timing windows of the first 10  $\mu\text{s}$  after the breakdown

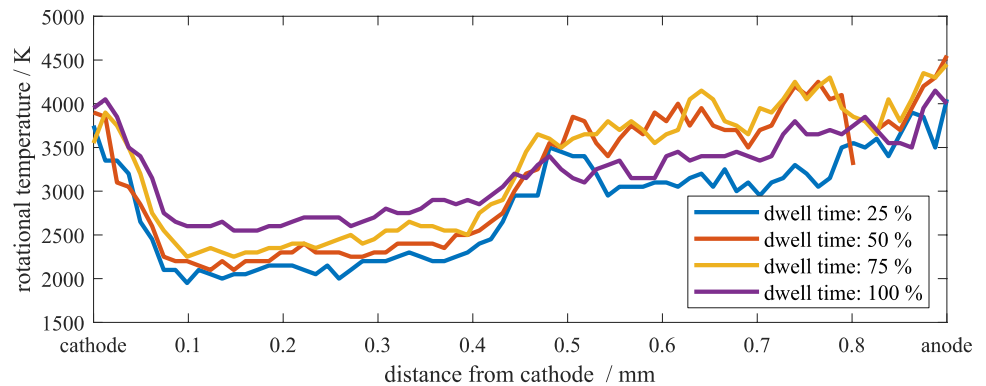
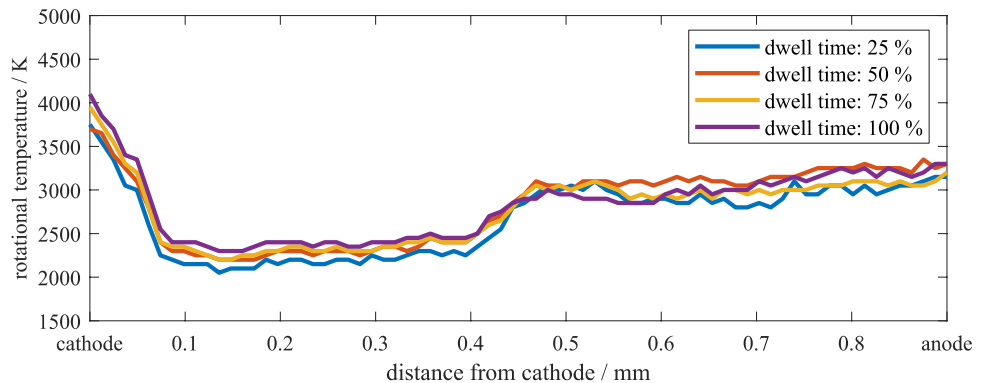


**Fig. 12** Rotational temperature during the glow phase at different positions in the discharge gap by varying the dwell time of the ignition coil. The temperature is averaged from the end of the arc phase to the end of the discharge



2400 K in the NG area. In this area the SNR is high, so a decrease with decreasing dwell time can be observed. In the FDS between 0.4 and 0.5 mm from the cathode the temperature increases from 2500 K, 2350 K, respectively, for a dwell time of 25%, to  $3000 \text{ K} \pm 250 \text{ K}$ . After FDS the PC of the glow discharge is located, which occupies the remaining spark gap. The trend of the intensity is similar to [62]. This area has a rotational temperature of 3000 K to  $3150 \text{ K} \pm 250 \text{ K}$ , independent from the dwell time. The trend of the rotational temperature is similar to the trend found in [44].

## 4 Discussion

During the breakdown, an effect of the short duration of the gate opening timing can be excluded due to the short life times of the  $C^3\Pi_u \rightarrow B^3\Pi_g \Delta v = 0$  transition of approx. 40 ns [29] and especially for rotational lifetimes of approx. 0.7 ns [2]. So, the majority of the emitted light due to the breakdown is measured. The low rotational temperature of 450 K of the breakdown is contrasted by a very high radiation density over the entire spark gap. Due to the constant value of the product of the pressure and the discharge gap ( $p \times d$ ), the static breakdown voltage is constant for all dwell times when applying the Paschen's law. With Eq. (6) and a constant capacity the supplied electric energy is constant. Therefore, no influence on the energy of the gas during the breakdown is expected and is confirmed by the measurements.

Compared to the breakdown the energy and duration of inductive arc depends directly from the dwell time of the coil. The less transferred energy leads to a decrease in the secondary inductive peak current. Due to this decrease the probability for an inductive arc decreases too. Therefore, only at the 100% dwell time the arc phase is analyzed. This arc has a higher temperature compared to the glow discharge in the first area between the spark gap. The temperature in the spark gap varies less than in the glow phase. This is due to the plasma physical model of an arc discharge which has only a PC and no NG or FDS [18]. Transitions between arc and glow discharges are observed during the measurements with 100% dwell time. An influence of this effect can be observed as the increase of rotational temperature in the last 0.4 mm to the anode. The capacitive arc discharge, with a duration of less than 1  $\mu\text{s}$ , is too short and therefore has a too low intensity of radiation to have a significance influence in the rotational temperature determination.

At ambient pressure, the glow discharge has the major part of the total spark duration. Its high temperature near the cathode might be due to fast electrons (observed by [28]), which are released from the cathode by the tunneling effect or secondary electron emission. To evaluate this theory, measurements with electrode materials with different work

functions should be performed in the future. Only a weak amount of radiation is measured in this area of the discharge. The following NG is the brightest area in this discharge. Due to a high decrease of the electron velocity by recombination and collisions [18], the rotational temperature decreases to values in the range of 2200–2400 K. A tendency of decreasing rotational temperature with decreasing dwell time can be suspected, but is within the measurement uncertainty. This could be due to a reduction in of the average current in this phase. A dependence, as it is observed, is in agreement with the literature [3, 61]. After the NG, the FDS occurs. This area is characterized by low radiation intensities. The electrons lose the most energy in the area of the NG. In the rotational temperature measurements, an increase in rotational temperature can be observed. Only a small number of electrons gain enough energy to excite the electronic  $C^3\Pi_u$  rotational levels, this leads to a low intensity of radiation. After the FDS, the PC with a slightly increased radiation is observed. It seems that more high rotational levels are excited in this area of the glow discharge. The rotational temperature is constant over the range of the PC. The tendency of higher rotational temperature in the PC compared to the NG is also observed in [4, 42, 68]. Two established explanation for this are the effect of scattering and the quadrupole effect. In dependence of the scattering angle, the excitation of higher rotational energy levels can occur [12, 14, 19, 51]. For homonuclear diatomic molecules, like the observed  $\text{N}_2$ , [15, 20] a higher interaction by the 'electron–quadrupole interaction' [20] is expected.

## 5 Conclusion and outlook

We showed and evaluated a method for special and temporal determination of the rotational temperature as an indicator of the gas temperature of ignition sparks at atmospheric pressure and room temperature. The measurements are performed with a variation of the dwell time of the ignition coil. A cold breakdown phase, with a rotational temperature of approx. 450 K, was calculated and reproducibly measured. Due to the long gate opening duration, regarding the breakdown, we expect lower rotational temperatures in the range of ambient temperature (in this case 300 K). Only with a dwell time of 100%, we observed an arc with enough energy to measure fragments of its rotational temperature which lies between 2700 and 4000 K. The rotational temperature of the glow discharge depends more strongly of the area between the spark gap. In the area near the cathode high temperatures of 4000 K are observed. In the negative glow the lowest temperatures with approx. 2300 K are calculated with the highest intensities. A rotational temperature increase in the Faraday dark space up to the values positive column (3000 K) was observed. This results in the ranking of the

rotational temperature  $T_{\text{Rot, Breakdown}} < T_{\text{Rot, Glow}} < T_{\text{Rot, Arc}}$ . By comparing this ranking with the ranking of the inflammation probability of Maly, the inflammation probability cannot only be a function of the rotational temperature, which represents the gas temperature. Additional studies must therefore be performed to better understand the inflammation process and to optimize ignition systems for the future.

Further investigations will follow in the future by varying the systems electrical parameters and under higher pressures and temperatures. Additional plasma temperatures such as vibrational and electron temperature as well as the electron density are to be determined. Furthermore, the influence on the cathode area in the glow discharge is to be determined with different electrode materials and diameters.

**Acknowledgements** Open Access funding provided by Projekt DEAL. This research work was conducted within the project “Profilregion Mobilitätssysteme Karlsruhe” funded by the “Ministerium für Wissenschaft, Forschung und Kunst und das Ministerium für Finanzen und Wirtschaft des Landes Baden-Württemberg”. The authors express their thanks to them and all the project partners involved.

**Open Access** This article is licensed under a Creative Commons Attribution 4.0 International License, which permits use, sharing, adaptation, distribution and reproduction in any medium or format, as long as you give appropriate credit to the original author(s) and the source, provide a link to the Creative Commons licence, and indicate if changes were made. The images or other third party material in this article are included in the article’s Creative Commons licence, unless indicated otherwise in a credit line to the material. If material is not included in the article’s Creative Commons licence and your intended use is not permitted by statutory regulation or exceeds the permitted use, you will need to obtain permission directly from the copyright holder. To view a copy of this licence, visit <http://creativecommons.org/licenses/by/4.0/>.

## References

- Ceviz, M.A., Sen, A.K., Küleri, A.K., Öner, İ.V.: Engine performance, exhaust emissions, and cyclic variations in a lean-burn SI engine fueled by gasoline–hydrogen blends. *Appl. Therm. Eng.* **36**, 314–324 (2012). <https://doi.org/10.1016/j.applthermaeng.2011.10.039>
- Arkhipenko, V.I., Zgurovskii, S.M., Kirillov, A.A., Simonchik, L.V.: Cathode fall parameters of a self-sustained normal glow discharge in atmospheric-pressure helium. *Plasma Phys. Rep.* **28**, 858–865 (2002). <https://doi.org/10.1134/1.1513839>
- Arkhipenko, V.I., Kirillov, A.A., Safronau, Y.A., Simonchik, L.V., Zgurovskii, S.M.: Self-sustained dc atmospheric pressure normal glow discharge in helium: from microamps to amps. *Plasma Sources Sci. Technol.* **18**, 45013 (2009). <https://doi.org/10.1088/0963-0252/18/4/045013>
- Arkhipenko, V.I., Kirillov, A.A., Safronau, Y.A., Simonchik, L.V., Zgurovskii, S.M.: Plasma non-equilibrium of the DC normal glow discharges in atmospheric pressure atomic and molecular gases. *Eur. Phys. J. D* **66**, 252 (2012). <https://doi.org/10.1140/epjd/e2012-30359-x>
- Bauer, A.: Zur Theorie des Kathodenfalls in Lichtbögen. *Zeitschrift für Physik* **138**, 35–55 (1954). <https://doi.org/10.1007/BF01365533>
- Bauer, A., Schulz, P.: Elektrodenfälle und Bogengradienten in Hochdruckentladungen, insbesondere bei Xenon. *Zeitschrift für Physik* **139**, 197–211 (1954). <https://doi.org/10.1007/BF01375261>
- Bauer, H., Gollin, W.: Zündung im Ottomotor, Gelbe Reihe: Fachwissen Kfz-Technik: Motorsteuerung für Ottomotoren, 1st edn. Robert Bosch GmbH, Stuttgart (2002)
- Baus, S.: Funkenerosionsmodell von Nickelbasislegierungen. Saarbrücker Reihe Materialwissenschaft und Werkstofftechnik, 24th edn. Shaker, Aachen (2011)
- Chen, W., Madison, D., Dice, P., Naber, J., Chen, B., Miers, S., Czekala, M., Glugla, C., Qu, Q., Huberts G.: Impact of ignition energy phasing and spark gap on combustion in a homogenous direct injection gasoline SI engine near the EGR limit. In: SAE Technical Paper Series. SAE International400 Commonwealth Drive, Warrendale, PA, United States (2013)
- Cicala, G., De Tommaso, E., Rainò, A.C., Lebedev, Y.A., Shakhmatov, V.A.: Study of positive column of glow discharge in nitrogen by optical emission spectroscopy and numerical simulation. *Plasma Sources Sci. Technol.* **18**, 25032 (2009). <https://doi.org/10.1088/0963-0252/18/2/025032>
- Dale, J.D., Checkel, M.D., Smy, P.R.: Application of high energy ignition systems to engines. *Prog. Energy Combust. Sci.* **23**, 379–398 (1997). [https://doi.org/10.1016/S0360-1285\(97\)00011-7](https://doi.org/10.1016/S0360-1285(97)00011-7)
- Dalgarno, A.: Inelastic collisions at low energies. *Can. J. Chem.* **47**, 1723–1729 (1969). <https://doi.org/10.1139/v69-284>
- Dushman, S.: Electron emission from metals as a function of temperature. *Phys. Rev.* **21**, 623–636 (1923). <https://doi.org/10.1103/PhysRev.21.623>
- Ehrhardt, H., Linder, F.: Rotational excitation of H<sub>2</sub> by slow electrons in a beam experiment. *Phys. Rev. Lett.* **21**, 419–421 (1968). <https://doi.org/10.1103/PhysRevLett.21.419>
- Engelhardt, A.G., Phelps, A.V., Risk, C.G.: Determination of momentum transfer and inelastic collision cross sections for electrons in nitrogen using transport coefficients. *Phys. Rev.* **135**, A1566–A1574 (1964). <https://doi.org/10.1103/PhysRev.135.A1566>
- European Commission (2018a) 2030 climate and energy package. [https://ec.europa.eu/clima/policies/strategies/2030\\_en](https://ec.europa.eu/clima/policies/strategies/2030_en). Accessed 4 Sept 2019
- European Commission (2018b) A clean planet for all: a European strategic long-term vision for a prosperous, modern, competitive and climate neutral economy. <https://eur-lex.europa.eu/legal-content/EN/TXT/?uri=CELEX:52018DC0773>. Accessed 4 Sept 2019
- Fridman, A., Kennedy, L.A.: *Plasma Physics and Engineering*, 2nd edn. CRC Press, Hoboken (2011)
- Gerjuoy, E., Stein, S.: Rotational excitation by slow electrons. *Phys. Rev.* **97**, 1671–1679 (1955). <https://doi.org/10.1103/PhysRev.97.1671>
- Golden, D.E., Lane, N.F., Temkin, A., Gerjuoy, E.: Low energy electron-molecule scattering experiments and the theory of rotational excitation. *Rev. Mod. Phys.* **43**, 642–678 (1971). <https://doi.org/10.1103/RevModPhys.43.642>
- Graff, M., Kempf, B., Breme, J.: Abbrandfeste Iridium-Legierung für Zündkerzenelektroden. *Metall* **53**, 616–621 (1999)
- Grtmley, H.M., Emeleus, K.G.: Note on secondary electrons in the negative glow and faraday dark space. *Int. J. Electron.* **22**, 487–494 (1967). <https://doi.org/10.1080/00207216708937983>
- Güntherschulze, A.: Die Abhängigkeit des normalen Kathodenfalles der Glimmentladung von der Gasdichte. *Zeitschrift für Physik* **49**, 473–479 (1928). <https://doi.org/10.1007/BF01333631>
- Güntherschulze, A.: Zusammenhang zwischen Stromdichte und Kathodenfall der Glimmentladung bei Verwendung einer Schutzringkathode und Korrektur der Temperaturerhöhung des Gases. *Zeitschrift für Physik* **49**, 358–379 (1928). <https://doi.org/10.1007/BF01337924>

25. Günther-Schulze, A.: Kathodenfall, Ionisierungsspannung und Atomgewicht. *Zeitschrift für Physik* **20**, 153–158 (1923). <https://doi.org/10.1007/BF01327928>
26. Hurt, W.B.: The Faraday dark space of a glow discharge. *Am. J. Phys.* **37**, 47–51 (1969). <https://doi.org/10.1119/1.1975402>
27. Iza, F., Hopwood, J.A.: Rotational, vibrational, and excitation temperatures of a microwave-frequency microplasma. *IEEE Trans. Plasma Sci.* **32**, 498–504 (2004). <https://doi.org/10.1109/TPS.2004.826145>
28. Jiang, W., Tang, J., Wang, Y., Zhao, W., Duan, Y.: Characterization of argon direct-current glow discharge with a longitudinal electric field applied at ambient air. *Sci. Rep.* **4**, 6323 (2014). <https://doi.org/10.1038/srep06323>
29. Johnson, A.W., Fowler, R.G.: Measured lifetimes of rotational and vibrational levels of electronic states of N<sub>2</sub>. *J. Chem. Phys.* **53**, 65–72 (1970). <https://doi.org/10.1063/1.1673834>
30. Kim W., Bae C., Michler T., Toedter O., Koch T.: Spatio-temporally resolved emission spectroscopy of inductive spark ignition in atmospheric air condition. In: Ignition systems for gasoline engines: 4th international conference, December 6–7, 2018, Berlin, Germany. Eds.: M. Günther, pp. 209–221 (2018)
31. Kramer, U., Orloff, F., Stollenwerk, S.: Defossilisierung des Transportsektors: Optionen und Voraussetzungen in Deutschland. Forschungsvereinigung Verbrennungskraftmaschinen R, FVV, Deutschland (2018)
32. Kühler, A.: Hochspannungstechnik: Grundlagen, Technologie, Anwendungen, VDI-Buch, 3rd edn. Springer, Berlin (2009)
33. Lichtenberg, S.: Charakterisierung von Elektroden für Hochdruck-Plasmalampen durch elektrische Messungen und Modellierungen, vol. 7. Tenea Verlag Ltd, Berlin (2004)
34. Lino da Silva, M.: An adaptive line-by-line—statistical model for fast and accurate spectral simulations in low-pressure plasmas. *J. Quant. Spectrosc. Radiat. Transfer* **108**, 106–125 (2007)
35. Lino da Silva, M.: A contribution for the simulation of VUV-IR radiation transfer in CO<sub>2</sub>–N<sub>2</sub> entry flows using a line-by-line model. In: Radiation of High Temperature Gases in Atmospheric Entry, vol. 686 (2011)
36. Linss, V., Kupfer, H., Peter, S., Richter, F.: Two N<sub>2</sub> textem-dashimproved estimation of the neutral gas temperature. *J. Phys. D Appl. Phys.* **37**, 1935–1944 (2004). <https://doi.org/10.1088/0022-3727/37/14/008>
37. Loeb, L.B.: Basic processes of gaseous electronics. University of California, Berkeley (1955)
38. Lüdi, F.: Über den Mechanismus der Elektronenauslösung im Kathodenfleck einer Bogenentladung. *Zeitschrift für Physik* **82**, 815–832 (1933). <https://doi.org/10.1007/BF01334131>
39. Maly, R., Albrecht, H., Bloss, W.H., Herden, W., Saggau, B., Wagner, E.: Neue Ergebnisse über die Entflammung durch den elektrischen Funken. In: 4th Satusseminar Kraftfahrzeug- und Straßenverkehrstechnik (1977)
40. Maly, R., Herden, W., Saggau, B., Wagner, E., Vogel, M., Bauer, G., Bloss, W.H.: Die drei Phasen einer elektrischen Zündung und ihre Auswirkungen auf die Entflammungseinleitung. In: 5th Satusseminar Kraftfahrzeuge und Straßenverkehr (1978)
41. Maly, R., Vogel, M.: Initiation and propagation of flame fronts in lean CH<sub>4</sub>-air mixtures by the three modes of the ignition spark. *Symp. Int. Combust.* **17**, 821–831 (1979). [https://doi.org/10.1016/s0082-0784\(79\)80079-x](https://doi.org/10.1016/s0082-0784(79)80079-x)
42. Maximov, A.I., Khlustova, A.V.: Optical emission from plasma discharge in electrochemical systems applied for modification of material surfaces. *Surf. Coat. Technol.* **201**, 8782–8788 (2007). <https://doi.org/10.1016/j.surfcoat.2007.02.042>
43. Meek, J.M., Craggs, J.D. (eds.): Electrical breakdown of gases: the international series of monographs on physics. Clarendon Press, Oxford (1953)
44. Mezei, P., Cserfalvi, T., Csillag, L.: The spatial distribution of the temperatures and the emitted spectrum in the electrolyte cathode atmospheric glow discharge. *J. Phys. D Appl. Phys.* **38**, 2804–2811 (2005). <https://doi.org/10.1088/0022-3727/38/16/010>
45. Michler, T., Kim, W., Toedter, O., Koch, T., Bae, C.: Influence of the electrical parameters of the ignition system on the phases of spark ignition. In: ignition systems for gasoline engines. In: 4th International Conference, December 6–7, 2018, Berlin, Germany. Ed.: M. Günther. expert Verlag, Tübingen, pp. 222–238 (2018a)
46. Michler, T., Kim, W., Toedter, O., Koch, T., Bae, C.: Influence of the electrical parameters of the ignition system on the phases of spark ignition. In: ignition systems for gasoline engines. In: 4th International Conference, December 6–7, 2018, Berlin, Germany. Ed.: M. Günther. expert Verlag, Tübingen, pp. 222–238 (2018b)
47. Myer, J.L.: Sondenmessungen am Lichtbogen in Luft bei atmosphärischem Druck. *Zeitschrift für Physik* **87**, 1–18 (1934). <https://doi.org/10.1007/BF01338445>
48. Oshima, M.: Determination of plasma gas temperature during reactive sputter etching. *Jpn. J. Appl. Phys.* **17**, 1157–1158 (1978). <https://doi.org/10.1143/jjap.17.1157>
49. Paschen, F.: Ueber die zum Funkenübergang in Luft, Wasserstoff und Kohlensäure bei verschiedenen Drucken erforderliche Potentialdifferenz. *Ann. Phys.* **273**, 69–96 (1889). <https://doi.org/10.1002/andp.18892730505>
50. Peters, F.: Vergleich dielektrisch behinderter Entladungen bezüglich der physikalischen Eigenschaften und der Wirkung auf Holz und Holzwerkstoffe. Dissertation, Georg-August-Universität Göttingen (2018)
51. Phelps, A.V.: Rotational and vibrational excitation of molecules by low-energy electrons. *Rev. Mod. Phys.* **40**, 399–410 (1968). <https://doi.org/10.1103/RevModPhys.40.399>
52. Phillips, D.M.: Determination of gas temperature from unresolved bands in the spectrum from a nitrogen discharge. *J. Phys. D Appl. Phys.* **9**, 507–521 (1976). <https://doi.org/10.1088/0022-3727/9/3/017>
53. Potteau, S., Lutz, P., Leroux, S., Moroz, S., Tomas, E.: Cooled EGR for a turbo SI engine to reduce knocking and fuel consumption. In: SAE Technical Paper Series. SAE International/400 Commonwealth Drive, Warrendale, PA, United States (2007)
54. Raether, H.: Electron avalanches and breakdown in gases. Butterworths advanced physics series. Butterworths, London (1964)
55. Rager, J.: Funkenerosion an Zündkerzenelektroden: Saarbrücker Reihe Materialwissenschaft und Werkstofftechnik, 5th edn. Shaker, Aachen (2006)
56. Ramberg, W.: Über den Mechanismus des elektrischen Lichtbogens. *Ann. Phys.* **404**, 319–352 (1932). <https://doi.org/10.1002/andp.19324040305>
57. Rogowski, W.: Über Durchschlag und Gasentladung. *Z. Physik* **100**, 1–49 (1936). <https://doi.org/10.1007/BF01337744>
58. Rollwagen, W.: Die physikalischen Erscheinungen der Bogenentladung in ihrer Bedeutung für die spektralanalytischen Untersuchungsmethoden. In: Rollwagen, W. (ed.) Die physikalischen Erscheinungen der Bogenentladung in ihrer Bedeutung für die spektralanalytischen Untersuchungsmethoden, pp. 66–82. Springer, Berlin (1939)
59. Schottky, W.: Über spontane Stromschwankungen in verschiedenen Elektrizitätsleitern. *Ann. Phys.* **362**, 541–567 (1918). <https://doi.org/10.1002/andp.19183622304>
60. Shcherbakov, Y.V., Sigmond, R.S.: Subnanosecond spectral diagnostics of streamer discharges: I. Basic experimental results. *J. Phys. D Appl. Phys.* **40**, 460–473 (2007). <https://doi.org/10.1088/0022-3727/40/2/023>
61. Staack, D., Farouk, B., Gutsol, A.F., Fridman, A.A.: Spectroscopic studies and rotational and vibrational temperature measurements of atmospheric pressure normal glow plasma discharges in air.

- Plasma Sources Sci. Technol. **15**, 818–827 (2006). <https://doi.org/10.1088/0963-0252/15/4/027>
62. Staack, D., Farouk, B., Gutsol, A.F., Fridman, A.: Spatially resolved temperature measurements of atmospheric-pressure normal glow microplasmas in air. *IEEE Trans. Plasma Sci.* **35**, 1448–1455 (2007). <https://doi.org/10.1109/TPS.2007.904959>
63. Szwaja, S., Jamrozik, A., Tutak, W.: A two-stage combustion system for burning lean gasoline mixtures in a stationary spark ignited engine. *Appl. Energy* **105**, 271–281 (2013). <https://doi.org/10.1016/j.apenergy.2012.12.080>
64. Toulson, E., Schock, H.J., Attard, W.P.: A review of pre-chamber initiated jet ignition combustion systems. In: SAE Technical Paper Series. SAE International 400 Commonwealth Drive, Warrendale, PA, United States (2010)
65. Townsend, J.S.E.: *Electricity in gases*. Clarendon Press, Oxford (1915)
66. Townsend, J.S.E.: *Electrons in gases*. Hutchinson's scientific and technical publications, London (1947)
67. Townsend, J.S.E., Tizard, H.T.: The motion of electrons in gases. *Proc. R. Soc. A Math. Phys. Eng. Sci.* **88**, 336–347 (1913). <https://doi.org/10.1098/rspa.1913.0034>
68. Webb, M.R., Andrade, F.J., Gamez, G., McCrindle, R., Hieftje, G.M.: Spectroscopic and electrical studies of a solution-cathode glow discharge. *J. Anal. At. Spectrom.* **20**, 1218 (2005). <https://doi.org/10.1039/b503961d>
69. Zhou, M., Li, G., Liang, J., Ding, H., Zhang, Z.: Effect of ignition energy on the uncertainty in the determination of laminar flame speed using outwardly propagating spherical flames. *Proc. Combust. Inst.* **37**, 1615–1622 (2019). <https://doi.org/10.1016/j.proci.2018.07.084>

**Publisher's Note** Springer Nature remains neutral with regard to jurisdictional claims in published maps and institutional affiliations.